Minority-spin impurity band in math xmlns="http://www.w3.org/1998/Math/MathML">mi mathvariant="normal">n/mi>/math>-type (In,Fe)As: A materials perspective for ferromagnetic semiconductors

Masaki Kobayashi, Le Duc Anh, Jan Minár, Walayat Khan, Stephan Borek, Pham Nam Hai, Yoshihisa Harada, Thorsten Schmitt, Masaharu Oshima, Atsushi Fujimori, Masaaki Tanaka, and Vladimir N. Strocov

Phys. Rev. B **103**, 115111 — Published 8 March 2021

DOI: 10.1103/PhysRevB.103.115111

Minority-Spin Impurity Band in n-Type (In,Fe)As: A Materials Perspective for Ferromagnetic Semiconductors

Masaki Kobayashi[1,2,3,4,*], Le Duc Anh[4,5,6], Jan Minár[7], Walayat Khan[8], Stephan Borek[9], Pham Nam Hai[3,4,10], Yoshihisa Harada[11], Thorsten Schmitt[1], Masaharu Oshima[2], Atsushi Fujimori[12,13], Masaaki Tanaka[3,4], and Vladimir N. Strocov[1,]

[1]*Swiss Light Source, Paul Scherrer Institut, CH-5232 Villigen PSI, Switzerland*

[2]*Department of Applied Chemistry, School of Engineering, The University of Tokyo, 7-3-1 Hongo, Bunkyo-ku, Tokyo 113-8656, Japan*

[3]*Department of Electrical Engineering and Information Systems, The University of Tokyo, 7-3-1 Hongo, Bunkyo-ku, Tokyo 113-8656, Japan*

[4]*Center for Spintronics Research Network, The University of Tokyo, 7-3-1 Hongo, Bunkyo-ku, Tokyo 113-8656, Japan*

[5]*Institute of Engineering Innovation, Graduate School of Engineering, The University of Tokyo, 7-3-1 Hongo, Bunkyo-ku, Tokyo 113-8656, Japan*

[6]*PRESTO, JST, 4-1-8 Honcho, Kawaguchi, Saitama, 332-0012, Japan*

[7]*NewMaterials -Technologies: Research Centere, University of West Bohemia, Pilsen, Czech Rep.*

[8]*Bacha Khan University, Charsadda, KPK, Pakistan*

[9]*Deutsches Zentrum für Luft- und Raumfahrt (DLR), Oberpfaffenhofen, 82234 Weßling, Germany*

[10]*Department of Physical Electronics, Tokyo Institute of Technology, 2-12-1 Ookayama, Meguro-ku, Tokyo 152-0033, Japan*

[11]*Insititute for Solid State Physics, The University of Tokyo, 1-1-1 Koto, Sayo, Hyogo 679-5198, Japan*

[12]*Department of Physics, The University of Tokyo, 7-3-1 Hongo, Bunkyo-ku, Tokyo 113-0033, Japan*

[13]*Department of Applied Physics, Waseda University, Okubo, Shinjuku, Tokyo 169-8555, Japan*

*Email: masaki.kobayashi@ee.t.u-tokyo.ac.jp

(Date: February 13, 2021)

Abstract

Fully understanding the properties of *n-type* ferromagnetic semiconductors (FMSs), complementary to the mainstream p-type ones, is a challenging goal in semiconductor spintronics because ferromagnetism in n-type FMSs is theoretically non-trivial. Soft-x-ray angle-resolved photoemission spectroscopy (SX-ARPES) is a powerful approach to examine the mechanism of carrier-induced ferromagnetism in FMSs. Here our SX-ARPES study on the prototypical n-type FMS (In,Fe)As reveals the entire band structure including the Fe-3*d* impurity bands (IBs) and the host InAs ones, and provides direct evidence for electron occupation of the InAs-derived conduction band (CB). A minority-spin Fe-3*d* IB is found to be located just below the conduction-band minimum (CBM). The IB is formed by the hybridization of the unoccupied Fe 3*d* states with the

occupied CBM of InAs in a spin-dependent way, resulting in the large spin polarization of CB. The band structure with the IB is varied with band filling, which cannot be explained by the rigid-band picture, suggesting a unified picture for realization of carrier-induced ferromagnetism in FMS materials.

I. INTRODUCTION

Evolution of information technology has been driven by high-performance electronic devices based on high-quality semiconductor materials. Since the sophistication of semiconductor electronic devices by miniaturization has approached the technical limit, the development of new functional spin-based devices has been pursued [1, 2]. Spintronics is a research field aiming at manipulating and utilizing both the charge and spin degrees of freedom of carriers, and spintronic devices have a potential to dramatically reduce the power consumption and realize new functionalities related to the spin degree of freedom [1–5]. For instance, bilayer thin films consisting of a ferromagnetic layer and superconductors, topological insulators, or two-dimensional electron gas have recently attracted much attention for their novel spintronics functionalities, including the realization of Majorana Fermions for quantum computing [3]. To apply these spintronics functionalities to the well-established semiconductor technology, materials having both the semiconducting and ferromagnetic properties are highly desirable. Ferromagnetic semiconductors (FMSs), in which the cation sites in a

semiconductor crystal are partially replaced by magnetic atoms, bear a high promise for their applications in semiconductor spintronics [1-3] because of their capability to manipulate both the charge and spin degrees of freedom of carriers [4, 5]. FMSs are key materials to realize the practical application of the spin-related functionalities [1, 4-8].

Fundamental understanding of the origin or mechanism of ferromagnetism in FMSs is important for the application of the FMS materials to spintronics devices. It is known that the ferromagnetism in many FMSs is induced by doping carriers. In contrast to the traditional p-type Mn-doped FMSs such as (Ga,Mn)As, novel Fe-doped III-V FMSs have recently attracted much attention, because Fe-doped FMSs can accommodate both n- and p-type carriers and exhibit ferromagnetism with high Curie temperature T_C (> 300 K) [5, 9, 10]. Using the p-type and/or n-type Fe-doped FMSs, spintronics devices have already been demonstrated [6, 7, 11, 12]. $(In_{1-x},Fe_x)As$ co-doped with Be (referred to as (In,Fe)As:Be hereafter) is the first n-type FMS [13, 14], where the Be ions act as double donors [15]. (In,Fe)As:Be shows ferromagnetic properties when its electron-carrier concentration (n) is higher than 6×10^{18} cm^{-3} [13]. The findings of light electron effective mass [14] and large spin-splitting in the conduction-band minimum (CBM) Δ_{ex} [12] suggest that highly mobile conduction electrons are spin-polarized in the conduction band (CB) of (In,Fe)As:Be. Although the

carrier-induced ferromagnetic properties and band structure of (In,Fe)As have been intensively studied so far, the precise mechanism of the ferromagnetism still remains an enigma.

Knowledge of the electronic structure, which is composed of the band structure of the host semiconductor and the 3*d* impurity band (IB), is indispensable for understanding the mechanism of the ferromagnetism in FMSs. Theoretically, it was considered impossible or difficult to realize a zinc-blend n-type FMS due to the weak orbital mixing between the host *s* and impurity *d* orbitals [16]. In this Letter, we have investigated the band structure of the prototypical n-type FMS (In,Fe)As:Be using soft-X-ray angle-resolved photoemission spectroscopy (SX-ARPES) and spin-density-functional-theory (SDFT) calculation to understand the origin of the carrier-induced ferromagnetism. SX-ARPES is one of the most powerful experimental techniques to study the electronic structures of FMSs [17-20]. By using SX-ARPES, we reveal the entire band structure of (In,Fe)As:Be including the Fe-3*d* IB and electron occupation of the InAs-derived CB. Based on the experimental findings, we have identified that the Fe-3*d* IB located near CBM is formed by the hybridization of the CB and the Fe 3*d* state in a spin-dependent way, resulting in the large *s*-*d* exchange splitting in (In,Fe)As:Be. The underlying physics of the formation of the IB states in n-type

(In,Fe)As is found to be similar to that in p-type (Ga,Mn)As, providing a unified picture of ferromagnetism in FMSs irrespective of the carrier types. This suggests a materials perspective to realize the carrier-induced ferromagnetism in FMSs.

II. EXPERIMENTAL

$(In_{0.95},Fe_{0.05})As$:Be, $(In_{0.95},Fe_{0.05})As$, and InAs:Be thin films with a thickness of 20 nm were grown on InAs(001) substrates at 240 ^{o}C by molecular beam epitaxy. The Be concentrations were $\sim 2 \times 10^{19}$ cm^{-3}. In order to avoid surface oxidation, the thin films were covered by an amorphous As passivation layer with a thickness of ~1 nm. An As passivation layer for a GaAs layer hardly induces carrier depletion near the surface of the GaAs layer, thus band bending is negligible [21]. The SX-ARPES measurements were performed directly through the As capping layer due to the increase of probing depth in the SX region [22]. T_C of the $(In_{0.95},Fe_{0.05})As$:Be film was estimated to be ~40 K by the Arrott plot of the magnetic circular dichroism measurements. The SX-ARPES experiments were performed at the ADRESS beamline of SLS [23]. During the experiments, the samples were cooled to 10.7 K by liquid He to suppress the reduction of the coherent $\boldsymbol{k}$-resolved spectral component at high energies. The measurements were performed mostly at energy resolution $\Delta E \sim 120$ meV. Details of the SDFT calculations

are described in Appendix D.

III. SX-ARPES RESULTS

A. Fermi surface and band dispersion

SX-ARPES enables us to reveal bulk band structures of single-crystal materials with sharp definition of three-dimensional electron wavevector $\boldsymbol{k}$ [22]. Figure 1(a) shows the out-of-plane Fermi surface mapping (FSM) in the k_x-k_z plane of an $(In_{0.95}Fe_{0.05})As$:Be thin film. Here, the k_z and k_x directions are normal and parallel to the in-plane Γ-K-X symmetry line of the Brillouin zone, respectively. The mapping shows tiny but clear Fermi surface (FS) around the Γ points. As shown in Fig. 1(a), clear k_z dispersion of all the surface contours excludes the presence of any surface states that are identified by the absence of their k_z direction. This ensures that our SX-ARPES spectra truly reflect the bulk electronic structure of (In,Fe)As:Be.

Figure 1(b) shows an enlarged plot of the FS around the Γ point $[(k_x, k_z) = (-1.0, 15)\ \left(2\sqrt{2}\pi/a\right)]$. The cross-sections of the FS in the k_x-k_z out-of-plane as well as that in the k_x-k_y in-plane (not shown) are circular. Actually, the Fermi momenta are about 0.12 and 0.13 $Å^{-1}$ for the k_x and k_z directions, respectively. This suggests that the shape of the FS is spherical within the experimental accuracy. The carrier concentration

n estimated from the volume of the FS is $\sim 2 \times 10^{19}$ cm^{-3}; this value is above the threshold (6×10^{18} cm^{-3}) to induce the ferromagnetism in (In,Fe)As [13], and it is in good agreement with n estimated from the Hall measurement and is of the same order of magnitude as the concentration of co-doped Be. This result is consistent with the assumption that the Be dopant acts as a double donor in (In,Fe)As.

Figure 1(c) shows the band dispersion along the Γ-K-X line. Here, the incident photon energy $h\nu$ is set at 908 eV in order to bring the k_z value to the Γ point (see Fig. 1(a)). The hole-like band dispersions centered at Γ are the light-hole (LH) and split-off (SO) bands (see Appendix A for the heavy-hole (HH) band), and the electron-like one near the Fermi level (E_F) identifies the CB. As shown in Figs. 1(c) and 1(d), the CB dispersion clearly crosses E_F and forms the small FS so-called electron pocket (EP), consistent with the n-type conductivity confirmed by Hall-effect and thermoelectric Seebeck-effect measurements [13]. These results demonstrate that the electronic transport in ferromagnetic (In,Fe)As:Be arises from the electron carriers in the CB originating from the *s* band of InAs. This naturally explains their light effective mass [14] and the long mean-free path of electron carriers [11].

B. Fe 3*d*-derived impurity band in the band structure

In addition to the band dispersions, the location of the Fe-3*d* IB is also important to understand the ferromagnetism in (In,Fe)As. To identify the Fe-3*d* IB, we have employed resonant ARPES (rARPES) at the Fe L_3 edge. The resonant enhancement of the photoemission intensity occurs at $h\nu$ corresponding to the peaks of the Fe L_3 x-ray absorption spectroscopy (XAS) spectrum (Fig. 2(a)). Figure 2(b) shows the on- and off-resonance ARPES spectra measured with $h\nu = 708.2$ eV (the red arrow in Fig. 2(a)) and 705 eV (the black arrow), respectively. Note that, in addition to the intense Fe-3*d* IB (β-IB), a weak Fe-3*d* IB (α-IB) appears near CBM. The intensity of the α-IB is resonantly enhanced when $h\nu$ is at the peak of the XAS spectrum (see Fig. 2(a)), indicating that the α-IB is derived from the Fe 3*d* orbitals in (In,Fe)As, not from extrinsic Fe oxides. The β-IB results from the hybridization of the Fe 3*d* orbitals with the valence band (VB) and appears in the vicinity of the valence-band maximum (VBM). While the Mn-3*d* IB in (Ga,Mn)As splits off from VBM due to the strong *p-d* hybridization [17], the Fe-3*d* β-IB in (In,Fe)As does not. To elucidate the hybridization between the Fe 3*d* orbital and the ligand experimentally, the Fe-3*d* partial density of states (PDOS) corresponding to the difference between the on- and off-resonance spectra are plotted in Fig. 2(c). In addition to the $\boldsymbol{k}$-independent α-IB and β-IB, the PDOS around $k_x = -1.0$ $\left(2\sqrt{2}\pi/a\right)$ shows a dispersive feature corresponding to the

LH band (marked by vertical bars). Since the Fe 3*d* orbitals are independent of $\boldsymbol{k}$, the observation of dispersion in the PDOS evidences that the LH band is also resonantly enhanced at the Fe L_3 absorption edge through hybridization with the Fe 3*d* orbital.

C. Band structures of (In,Fe)As with and without carrier doping

The band structure of (In,Fe)As:Be revealed by SX-ARPES is summarized in Fig. 3(a), where the band dispersions along the Γ-K-X line are superimposed with the Fe-3*d* IBs. To separate the effects of Fe doping on the band structure of (In,Fe)As from that of Be, we have measured SX-ARPES spectra of the parent compound InAs:Be, as presented in Fig. 3(b). The EP around Γ also exists in InAs:Be. Comparing the band dispersions between InAs:Be and (In,Fe)As:Be, we find them nearly identical except for the presence of IBs in (In,Fe)As:Be. These results suggest that the electron carriers in (In,Fe)As:Be originate predominantly from the Be co-doping and not from the Fe doping. This indicates that the Fe^{3+} ions substitute for the In cation sites and provide the system with only the magnetic moments. To reveal the *n* dependence of the band structure, an paramagnetic $(In_{0.95},Fe_{0.05})As$ film without Be doping has been measured. Figure 3(c) shows the band structure measured on (In,Fe)As. One can see that both the EP and the α-IB disappear in the (In,Fe)As sample with a lower *n*. If the rigid-band

model is applicable, because the position of E_F is at or slightly below CBM in (In,Fe)As, the α-IB located just below CBM would be occupied, but it is not the case (see Fig. 3(c)). The present observation suggests that the location of the α-IB depends on n.

Based on these experimental findings, schematic views of the density of states (DOS) of ferromagnetic (In,Fe)As:Be and paramagnetic (In,Fe)As are shown in Figs. 4(a) and 4(b), respectively. It should be mentioned here that the concentration of the Be dopant is one to two orders of magnitude smaller than that of the Fe ions. If an in-gap Fe-3*d* IB exists below CBM, the amount of the supplied electrons by the Be doping was insufficient to fully occupy the IB and E_F would be located in the IB, not in the CB. Considering the appearance of the α-IB depending on n, the electron density of the α-IB located below E_F is presumably the same order of the Be dopant (10^{19} cm^{-3}), suggesting the partial occupation of the α-IB as shown in Fig. 4(a). This phenomenon looks analogous to the evolution of an IB state located below E_F with increasing K^+ concentration in K_xCo_{60} [24, 25]. A fundamental question here is why the partially filled α-IB is located below CBM in (In,Fe)As:Be despite the electron-carrier occupation of CBM.

D. SDFT calculations for (In,Fe)As

As shown in Fig. 2(a), the Fe L_3 XAS is characterized by a smooth and broad spectral peak without multiplet structure, which is similar to that of Fe metal or metallic Fe compounds (see Appendix B for details). Because the Fe 3*d* states in (In,Fe)As:Be are likely to be strongly covalent with ligand As *p* orbitals and are different from purely ionic Fe^{3+} [26], the broad spectral feature reflects the strong hybridization of the Fe 3*d* states with the ligand. As shown in Fig. 7 (see Appendix C), the SDFT calculations have demonstrated that the Fe 3*d* minority-spin (↓) states strongly hybridize with the ligand VB and CB states. Only the minority-spin states of the ligands hybridize with the unoccupied Fe 3*d* states, because the majority-spin (↑) 3*d* states are fully occupied and located well below the host VB. The β-IB originates from the hybridization between the Fe $3d_{\downarrow}$ states and the VBM states. Note that the calculated $e_{\downarrow}$ states show a slightly dispersive feature, indicating finite hybridization of the $e_{\downarrow}$ states with the minority-spin host band states. This result indicates that the hybridization between the $e_{\downarrow}$ and CBM states forms the α-IB just below CBM as shown in Fig. 4(d), if the hybridization is strong enough.

IV. Discussion

A. Formation of the Fe 3*d* IB through the *s*-*d* hybridization

When the CB is partially occupied, it is probable that the α-IB splits off from CBM through the s-$e_{\downarrow}$ hybridization, leading to the energy gap between the occupied and unoccupied α-IB states, as shown in Fig. 4(c). This partially filled split-off IB below E_F is similar to the formation of IB in the band gap observed in K_xC_{60}, where the IB is derived from electrons donated into the lowest unoccupied molecular orbital by the potassium [24, 25]. Additionally, emergence of the split-off IB related to the carrier-induced ferromagnetism is common feature to p-type FMS (Ga,Mn)As [17]. It should note here that the s-$e_{\downarrow}$ hybridization is spin-dependent in (In,Fe)As, that is, it happens only for the minority-spin states because the majority-spin states of Fe 3d are fully occupied. With the partially filled split-off α-IB, the minority-spin CBM loses states whereas the majority-spin one does not, as shown in Fig. 4(c).

The formation of the split-off state in the spin-dependent way results in a large spin-splitting Δ_{ex} of CBM in (In,Fe)As, as shown in Fig. 4(c). Indeed, the spin-splitting Δ_{ex} as large as 30–50 meV has been observed in n-(In,Fe)As/p-InAs Esaki-diode structures [12]. Based on the experimental findings, we have discussed qualitatively the origin of the large s-d exchange interaction. According to the Anderson Hamiltonian [27], the s-d exchange interaction $N_0\alpha$ is given by $|N_0\alpha| = -2|V_{sd}|^2\left(\frac{1}{E_C-\varepsilon_d}+\frac{1}{U-E_C+\varepsilon_d}\right)$,

where E_C is the energy of CBM, ε_d is the energy of the d states, U is the Coulomb repulsion between the d electrons, and V_{sd} is the s-d mixing potential [28]. From the value of T_C, $|N_0\alpha|$ for (In,Fe)As has been estimated to be ~2.8 eV [14], which is much larger than the p-d exchange interaction $|N_0\beta|$~1.2 eV in (Ga,Mn)As [29]. Since $|N_0\alpha|$ is inversely proportional to the energy difference $|E_C - \varepsilon_d|$ or $|U - E_C + \varepsilon_d|$, if one of the energy differences approaches zero, the value of $|N_0\alpha|$ will be significantly enhanced. This condition is referred to as the "resonance" condition [14]. As discussed above, while ε_d is well above E_C, the energy difference $|U - E_C + \varepsilon_d|$ is possibly small to satisfy the resonance condition in (In,Fe)As:Be. It follows from the above argument that the strong s-d exchange interaction $|N_0\alpha|$ [12, 14] leading to the carrier-induced ferromagnetism in (In,Fe)As:Be originates from the hybridization between the $e_\downarrow$ and CBM states, consistent with the large Δ_{ex} observed by tunneling spectroscopy [12].

B. Materials perspective for ferromagnetic semiconductors

The present results put forward important aspects for the materials design of FMSs. Generally, the ionicity of doped transition-metal ions will increase with the band gap of the host semiconductor [30]. Considering this tendency, the spin-dependent hybridization with the ligand would hardly occur in an FMS with a wide-gap

semiconductor. On the other hand, it has been pointed out theoretically that narrow-gap III-V semiconductors with strong covalency are appropriate for host compounds of both p-type and n-type FMSs [31, 32]. This scenario is consistent with the observations that n-type FMS (In,Fe)Sb with a smaller band gap shows higher T_C than (In,Fe)As:Be [10] and p-type (Ba,K)(Zn,Mn)$_2$As$_2$ has higher T_C than (Ga,Mn)As [33]. Since the split-off IB states originate from strong *s*-*d* or *p*-*d* hybridization, the band structures proposed in the present study are likely to be applicable to other FMSs based on narrow-gap semiconductors. Another important aspect here is that the band structure with the split-off IB changes with n. Then, additional carrier-doping is necessary to validate realization of carrier-induced ferromagnetism in FMSs aside from the transition-metal dopants acting as donors or acceptors like Mn ions in (Ga,Mn)As. For example, Mn-doped FMSs with narrow-gap II-VI semiconductors co-doped with donor dopants will be candidates for n-type FMSs. Many FMS materials without carrier doping have been found to be paramagnetic so far. The emergence of carrier-induced ferromagnetism in such FMSs should be re-examined with additional carrier doping.

One of the most intriguing features here is that the energy position of the α-IB depends on the CB filling, which means that the rigid-band picture is not applicable. The split-off α-IB through the *s*-*d* hybridization in n-type (In,Fe)As discussed below is

analogous to the split-off IB through the *p-d* hybridization in p-type (Ga,Mn)As [17], although the carrier type is different. Note that the strong hybridization is essential to form the split-off IB states in both the FMSs. As to the underlying physics, the formation of these IB states due to hybridization with ligands is also analogous to that of the Zhang-Rice singlet band [34, 35]. It is likely that the split-off IB can be formed in a spin-dependent way depending on *n* and strength of the *sp-d* hybridization. These arguments suggest that appearance of the hybridization-derived split-off IB states near the band edge of host semiconductor (VBM for *p*-type or CBM for *n*-type) is attributed to be a unified picture to realize carrier-induced ferromagnetism in FMS materials irrespective of the carrier type. To obtain further evidence for the unified picture for the carrier-induced ferromagnetism, systematic studies of p-type and n-typed FMSs are desirable.

V. CONCLUSION

In conclusion, we have conducted SX-ARPES measurements combined with SDFT calculations for the prototypical n-type FMS (In,Fe)As:Be in order to elucidate the nature of the n-type FMSs. The SX-ARPES reveals the entire band structure including the Fe-3*d* IBs and the host InAs bands, providing direct evidence for electron

occupation of the InAs-derived CB. The Fe-3*d* IB located near CBM is formed through the hybridization with the ligand, which is the origin of the carrier-induced ferromagnetism in n-type (In,Fe)As. When the electron carriers occupy the CB, the partially filled IB splits off from CBM leading to the large spin-polarization of the CB. The intriguing feature that its band structure is deformed depending on the band filling is unexpected from the ordinary rigid-band picture. The underlying physics of the formation of the split-off IB is found to be similar to that in p-type (Ga,Mn)As [17], suggesting a unified picture for realizing carrier-induced ferromagnetism in FMSs irrespective of the carrier types.

ACKNOWLEDGMENTS

This work was supported by Grants-in-Aid for Scientific Research (Nos. 15H02109, 17H04922, 18H05345) from JSPS, and CREST (JPMJCR1777) and PRESTO Program (JPMJPR19LB) of Japan Science and Technology Agency. J.M. and W.K. would like to thank the CEDAMNF (CZ.02.1.01/0.0/0.0/15_003/0000358) co-funded by the Ministry of Education, Youth and Sports of Czech Republic. This work was partially supported the Spintronics Research Network of Japan (Spin-RNJ). M.K. acknowledges support from the Japan Society for the Promotion of Science.

APPENDIX

A. Linear polarization dependence of the ARPES spectra

The intensity of band dispersion depends on the polarization of the incident X rays reflecting the matrix element effects [36] and symmetry of the bands: The LH and SO bands, and CBM of the host InAs can be observed with *p* polarization, and the heavy hole (HH) band with *s* polarization, as well as the polarization dependence of bands of GaAs [23, 37] (note, however, that the CBM of GaAs has not been observed in the previous study because E_F is located below the CBM in *p*-type GaAs). Figure 5 shows the ARPES spectrum along the Γ-K-X symmetry line taken with the *s* polarization. Only the HH band is clearly observed due to the matrix element effects. Since the linear polarization dependence of ARPES reflects the symmetry of the bands [36], the CBM observed only with *p* polarization has the same symmetry as the LH and SO bands, not as the HH band. Figure 6 shows Fe L_3 resonant ARPES spectra taken with the *s* polarization. Both the Fe 3*d* α- and β-IBs can be observed in the on-resonance spectrum, while the intensities of the IBs are small and only the HH band can be observed in the off-resonance spectrum. Both the α-IB and β-IB are active for the *p* and *s* polarizations, as shown in Figs. 2(b) and 6, indicating that the IBs possibly hybridize with the LH, HH,

and SO bands of InAs.

B. Spectral line shape of Fe L_3 XAS

As shown in Fig. 2(e), the Fe L_3 XAS spectrum shows a single peak around 708 eV with a small dip around $h\nu \sim 709.5$ eV, different from multiple structures observed in Fe oxides [38], and the spectral line shape resembles those of Fe metal [39] and Fe pnictides [40]. The pre-edge structure around $h\nu \sim 705$ eV comes from the In M_2 edge. Although the spectral feature is similar to that of Fe metal, our previous x-ray magnetic circular dichroism (XMCD) study confirms that the electronic structure of Fe in (In,Fe)As is different from Fe metal [26], excluding the possibility that the ferromagnetic property comes from aggregation of Fe metal clusters in (In,Fe)As. The negligibly weak signal of Fe oxide (at $h\nu \sim 709.5$ eV) indicates that the amorphous As passivation layer well protected the (In,Fe)As:Be layer from oxidation.

C. Spin-density-functional-theory calculations

To gain a basic insight into the band structure of (In,Fe)As:Be, we have performed SDFT calculations for the band structures of (In,Fe)As. Figures 7(a) and 7(b) show the calculated band dispersions of (In,Fe)As for spin-up (majority) and spin-down

(minority) states, respectively. Here, we focus on the spin-polarized states and their hybridization revealed by the SDFT calculation. The Fe 3*d* *e* minority-spin ($e_\downarrow$) band appears near the CBM in the calculation. Note that this $e_\downarrow$ band shows a weak but finite dispersion, suggesting that the CBM states hybridize with the Fe 3*d* orbitals. Comparison with experiment as discussed below indicates that the observed E_F is located just above the CBM (dash-dotted lines). Concomitantly, the down-spin states ($e_\downarrow$ and $t_{2\downarrow}$) should be shifted upwards to above E_F due to the on-site Coulomb interaction at the Fe site, which is necessary to keep the Fe *d*-electron count within the realistic range but cannot be properly taken into account in SDFT. Also, an IB originating from the hybridization between the $e_\downarrow$ and CBM states appears below E_F. In this scenario, the spin direction of the Fe-3*d* IB is opposite to the total magnetization, consistent with the observation of the spin-Esaki diode behavior using (In,Fe)As [12]. As shown in Fig. 1(b), the Fe 3*d* t_2 minority-spin states strongly hybridize with the VB states of the InAs host below E = –2 eV (the p-$t_{2\downarrow}$ state). To see quantitatively how strongly the Fe 3*d* states are hybridized with the InAs band, the total density of states (DOS) and Fe 3*d* PDOS are plotted in Figs. 7(c) and 7(d), respectively. The Fe 3*d* minority-spin states obviously contribute to the VBM states, while the majority-spin band is largely located in the lower part of the VB (well below E = –3.5 eV) and has only negligible

contributions to the VBM. Therefore, the SDFT calculation indicates that the minority-spin Fe 3*d* states strongly hybridize with the ligand VB and conduction band. As discussed in the main text, the result that the dispersive feature of the $e_{\downarrow}$ band originating the hybridization with the CB is a key to understand the band structure of (In,Fe)As:Be and the appearance of the α-IB.

D. Details of the calculation

For the SDFT calculation of the electronic structure of $In_{0.9}Fe_{0.1}As$, we applied the all-electron augmented plane wave + local orbitals WIEN2K code. We employ the Engel-Vosko parameterization of a generalized gradient approximation (EV-GGA) [41]. This function has been successfully used in the past in studies of electronic band structure and density of states of InAs. Calculations for $In_{1-x}Fe_xAs$ has been performed within the supercell of 64 atoms, which nominally corresponds to x = 0.3125. The Brillouin zone was sampled by $5 \times 5 \times 5$ mesh. The wave functions in the atomic spheres were expanded up to an angular momentum of l_{max} = 10. The plane wave cutoff in the interstitial region was set so that $R_{MT} \times K_{MAX}$ = 7 and the energy and charge convergence was set to 10^{-4} eV. Here, R_{MT} and K_{MAX} are the smallest atomic sphere radius and the largest K-vector of the plane wave expansion of the wave function, and

the product $R_{MT} \times K_{MAX}$ describes the quality of the basis set used in the linearized augmented plane wave (LAPW) method.

E. SX-ARPES spectra of InAs:Be

The SX-ARPES spectra of an InAs:Be thin film was measured to compare with those of the ferromagnetic (In,Fe)As:Be thin film. Figure 8 shows the Fermi surface mapping (FSM) of the InAs:Be film. The in-plane and out-of-plane FSMs indicate that the shape of the electron Fermi surface in InAs:Be is spherical within the experimental accuracy like (In,Fe)As:Be shown in Fig. 1(b). Its Fermi momentum in the InAs:Be film is 1.16 times larger than that in the (In,Fe)As:Be film, indicating that the electron carrier concentration is ~3×10^{19} cm^{-3}, which is twice larger than the Be concentration. This result suggests that the Be dopant also acts as a double donor in parent InAs without Fe.

Figures 9(a) and 9(c) show the band dispersion along the Γ-K-X symmetry line taken with *p* and *s* polarizations, respectively. As shown in Fig. 9(a) taken with *p* polarization, the hole-like band dispersions centered at the Γ point are the LH and SO bands, and the electron-like one near E_F centered at Γ is the conduction band. As shown in Fig. 9(c), the SX-ARPES spectrum taken with the *s* polarization shows only the HH band due to the matrix element effects. The band dispersions along the Γ-K-X

symmetry line, as shown in Figs. 9(b) and 9(d), indicate that the EP can be seen only in the spectrum taken with *p*-polarization. The polarization dependence observed in InAs:Be is the same as that in (In,Fe)As:Be. Because the carrier concentration of the InAs:Be thin film is higher than that of the (In,Fe)As:Be one, the entire band dispersions of the InAs:Be are shifted downward compared with those of the (In,Fe)As:Be.

F. SX-ARPES spectra of paramagnetic (In,Fe)As

The paramagnetic (In,Fe)As thin film without Be doing has a low electron carrier concentration below the threshold to induce ferromagnetism. Figure 10 shows the band dispersion of paramagnetic (In,Fe)As. There is no intensity near E_F at the Γ point. Additionally, the entire band dispersions shift toward E_F compared with those of the Be doped films, consistent with the low carrier concentration of the paramagnetic (In,Fe)As. The quality of the data is lower than these of the (In,Fe)As:Be and InAs:Be thin films, because the thickness of the amorphous As capping layer on the (In,Fe)As thin film is thicker, and the thick capping layer weakens the ARPES signals. As shown in Fig. 3(a) and 3(c) (see the edges of VB and/or CB in the EDCs at Γ), the VBM of (In,Fe)As is located around $E_B \sim 0.6$ eV, indicating that the band gap is larger than ~0.6 eV, while the

band gap of (In,Fe)As:Be estimated from the energy difference between the VBM and CBM is ~0.54 eV. This result indicates that the band gap of (In,Fe)As:Be shrink compared to that of (In,Fe)As. Similar shrinking of the bandgap observed in K_3C_{60} compared to C_{60} has been explained as an effect beyond the one-electron potential approximation [42]. In contrast to insulating C_{60}, a conduction electron is well screened by carriers in metallic K_3C_{60}. This leads to the decrease of the band gap with increasing the carrier concentration. Thus, it is likely that the band gap of conducting (In,Fe)As:Be smaller than that of semiconducting (In,Fe)As originates from the same effect.

rARPES enables us to identify the Fe-3*d* IB states in (In,Fe)As. Figure 11 shows the Fe L_3 rARPES spectra of the paramagnetic (In,Fe)As thin film taken with *p* and *s* polarizations. It should be noted that there is no Fe-3*d* α-IB near E_F although the Fe-3*d* β-IB appears in the valence band at the resonance. Considering the observations of (In,Fe)As:Be, the results indicate that the appearance of the Fe-3*d* α-IB located near the conduction-band minimum depends on the carrier concentration, as discussed in the main text.

References

[1] H. Ohno, Science **281**, 951 (1998).
[2] S. A. Wolf, D. D. Awschalom, R. A. Buhrman, J. M. Daughton, S. von Molnár, M. L. Roukes, A. Y. Chtchelkanova, and D. M. Treger, Science **294**, 1488 (2001).
[3] I. Žutić, A. Matos-Abiague, B. Scharf, H. Dery, and K. Belashchenko, Mater. Today

22, 85 (2019).
[4] T. Dietl, Nat. Mater. **9**, 965 (2010).
[5] M. Tanaka, S. Ohya, and P. N. Hai, Appl. Phys. Rev. **1**, 011102 (2014).
[6] T. Nakamura, L. D. Anh, Y. Hashimoto, S. Ohya, M. Tanaka, and S. Katsumoto, Phys. Rev. Lett. **122**, 107001 (2019).
[7] K. Takiguchi, L. D. Anh, T. Chiba, T. Koyama, D. Chiba and M. Tanaka, Nat. Phys. **15**, 1134 (2019).
[8] N. H. D. Khang, and P. N. Hai, J. Appl. Phys. **126**, 233903 (2019).
[9] N. T. Tu, P. N. Hai, L. D. Anh, and M. Tanaka, Appl. Phy.s Lett. **108**, 192401 (2016).
[10] A. V. Kudrin, Yu. A. Danilov1, V. P. Lesnikov, M. V. Dorokhin, O. V. Vikhrova, D. A. Pavlov, Yu. V. Usov, I. N. Antonov, R. N. Kriukov, A. V. Alaferdov, and N. A. Sobolev, J. Appl. Phys. **122**, 183901 (2017).
[11] L. D. Anh, P. N. Hai, Y. Kasahara, Y. Iwasa, and M. Tanaka, Phys. Rev. B **92**, 161201(R) (2015).
[12] L. D. Anh, P. N. Hai, and M. Tanaka, Nat. Comm. **7**, 13810 (2016).
[13] P. N. Hai, L. D. Anh, S. Mohan, T. Tamegai, M. Kodzuka, T. Ohkubo, K. Hono, and M. Tanaka, Appl. Phys. Lett. **101**, 182403 (2012).
[14] P. N. Hai, L. D. Anh, and M. Tanaka, Appl. Phys. Lett. **101**, 252410 (2012).
[15] N. D. Vu, T. Fukushima, K. Sato, and H. Katayama-Hoshida, Jpn. J. Appl. Phys. **53**, 110307 (2014).
[16] T. Dietl, H. Ohno, and F. Matsukura, Phys. Rev. B **63**, 195205 (2001).
[17] M. Kobayashi, I. Muneta, Y. Takeda, Y. Harada, A. Fujimori, J. Krempasky, T. Schmitt, S. Ohya, M. Tanaka, M. Oshima, and V. N. Strocov, Phys. Rev. B **89**, 205204 (2014).
[18] J. Krempasky, S. Muff, F. Bisti, M. Fanciulli, H. Volfová, A.P. Weber, N. Pilet, P. Warnicke, H. Ebert, J Braun, F. Bertran, V. V. Volobuev, J. Minár, G. Springholz, J. H. Dil, and V. N. Strocov, Nat. Comm. **7**, 13071 (2016).
[19] S. Sakamoto, Y. K. Wakabayashi, Y. Takeda, S.-i. Fujimori, H. Suzuki, Y. Ban, H. Yamagami, M. Tanaka, S. Ohya, and A. Fujimori, Phys. Rev. B **95**, 075203 (2017).
[20] T. Takeda, M. Suzuki, L. D. Anh, N. T. Tu, T. Schmitt, S. Yoshida, M. Sakano, K. Ishizaka, Y. Takeda, S.-I. Fujimori, M. Seki, H. Tabata, A. Fujimori, V. N. Strocov, M. Tanaka, and M. Kobayashi, Phys. Rev. B **101**, 155142 (2020).
[21] N. J. Kawai, T. Nakagawa, T. Kojima, K. Ohta, M. Kawashima, Electron. Lett. **20**, 47 (1984).
[21] V. N. Strocov, L. L. Lev, M. Kobayashi, C. Cancellieri, M.-A. Husanua, A. Chikina, N. B. M. Schröter, X. Wanga, J. A. Krieger, and Z. Salman, J. Electron Spectrosc. Relat. Phenom. **236**, 1 (2019).
[23] V. N. Strocov, X. Wang, M. Shi, M. Kobayashi, J. Krempasky, C. Hess, T. Schmitt and L. Patthey, J. Synchrotron Rad. **21**, 32 (2014).
[24] G. K. Wertheim, J. E. Rowe, D. N. E. Buchanan, E. E. Chaban, A. F. Hebard, A. R. Kortan, A. V. Makhija, and R. C. Haddon, Science **252**, 1419 (1991).
[25] J. H. Weaver, P. J. Benning, F. Stepniak, and D. M. Poirier, J. Phys. Chem. Solids **53**, 1707 (1992).
[26] M. Kobayashi, L. D. Anh, P. N. Hai, Y. Takeda, S. Sakamoto, T. Kadono, T. Okane, Y. Saitoh, H. Yamagami, Y. Harada, M. Oshima, M. Tanaka, and A. Fujimori, Appl. Phys. Lett. **105**, 032403 (2014).
[27] P. W. Anderson, Phys. Rev. **124**, 41 (1964).

[28] J. R. Schrieffer, and P. A. Wolff, Phys. Rev. **149**, 491 (1966).
[29] J. Okabayashi, A. Kimura, O. Rader, T. Mizokawa, A. Fujimori, T. Hayashi, and M. Tanaka, Phys. Rev. B **58**, R4211 (1998).
[30] P. Manca, J. Phys. Chem. Solids **20**, 268 (1961).
[31] B. Gu, and S. Maekawa, Phys. Rev. B **94**, 155202 (2016).
[32] K. Sato, L. Bergqvist, J. Kudrnovský, P. H. Dederichs, O. Eriksson, I. Turek, B. Sanyal, G. Bouzerar, H. Katayama-Yoshida, V. A. Dinh, T. Fukushima, H. Kizaki, and R. Zeller, Rev. Mod. Phys. **82**, 1633 (2010).
[33] K. Zhao, Z. Deng, X. C. Wang, W. Han, J. L. Zhu, X. Li, Q. Q. Liu, R. C. Yu, T. Goko, B. Frandsen, Lian Liu, Fanlong Ning, Y. J. Uemura, H. Dabkowska, G. M. Luke, H. Luetkens, E. Morenzoni, S. R. Dunsiger, A. Senyshyn, P. Böni and C. Q. Jin, Nat. Comm. **4**, 1442 (2013).
[34] F. C. Zhang, and T. M. Rice, Phys. Rev. B **37**, 3759 (1988).
[35] K. Tsutsui, T. Tohyama, and S. Maekawa, Phys. Rev. Lett. **83**, 3705 (1999).
[36] A. Damascelli, Z. Hussain, Z.-X. Shen, Rev. Mod. Phys. **75**, 473 (2003).
[37] M. Kobayashi, I. Muneta, T. Schmitt, L. Patthey, S. Ohya, M. Tanaka, M. Oshima, and V. N. Strocov, Appl. Phys. Lett. **101**, 242103 (2012).
[38] T. Kataoka, M.Kobayashi, G. S. Song, Y. Sakamoto, A. Fujimori, F.-H. Chang, H.-J. Lin, D. J. Huang, C. T. Chen, S. K. Mandal, T. K. Nath, D. Karmakar, and I. Dasgupta, Jpn. J. Appl. Phys. **48**, 04C200 (2009).
[39] C. T. Chen, Y. U. Idzerda, H.-J. Lin, N. V. Smith, G. Meigs, E. Chaban, G. H. Ho, E. Pellegrin, and F. Sette, Phys. Rev. Lett. **75**, 152 (1995).
[40] W. L. Yang, A. P. Sorini, C-C. Chen, B. Moritz, W.-S. Lee, F. Vernay, P. Olalde-Velasco, J. D. Denlinger, B. Delley, J.-H. Chu, J. G. Analytis, I. R. Fisher, Z. A. Ren, J. Yang, W. Lu, Z. X. Zhao, J. van den Brink, Z. Hussain, Z.-X. Shen, and T. P. Devereaux, Phys. Rev. B **80**, 014508 (2009).
[41] E. Engel and S. H. Vosko, Phys. Rev. B **50**, 10498 (1994).
[42] T. Takahashi, S. Suzuki, T. Morikawa, H. Katayama-Yoshida, S. Hasegawa, H. Inokuchi, K. Seki, K. Kikuchi, S. Suzuki, K. Ikemoto, and Y. Achiba, Phys. Rev. Lett. **68**, 1232 (1992).

Figure legend

FIG.1. SX-ARPES spectra of (In,Fe)As:Be. (a) FSM in the k_z-k_x plane. k_x indicates the momentum along the Γ-K-X ([110]) direction. The solid curves are ***k***-space cuts for fixed $h\nu$. (b) Enlarged plot near the Γ point [$k_z = 15$ (2π/c)]. The top and right plots are momentum distribution curves along the k_x and k_z cuts across the Γ point (dashed lines), respectively. (c) APRES intensity along the Γ-K-X line obtained at $h\nu = 908$

eV. The inset is a blow-up of the EP. (d) Energy distribution curves (EDCs) around the Γ point.

FIG.2. Resonant ARPES spectra of (In,Fe)As:Be. (a) Fe L_3 XAS spectrum. The constant-initial-state (CIS) spectrum at $E_B = 0.25$ eV corresponding to the α-IB is also plotted. The arrows denote the excitation energies for rARPES. (b) Fe L_3 rARPES spectra. The left and right panels are the off- and on-resonance spectra, respectively. α- and β-IBs are Fe 3d-derived impurity bands. (c) EDCs of the rARPES spectra. (Top) On- and off-resonance EDCs at $k_x = -1.0$. (Bottom) Differences of the EDCs corresponding to the Fe-3d PDOS at various k_x. The vertical bars indicate a dispersive peak.

FIG.3. Comparison of band structures of (In,Fe)As with and without doping. (a) Band dispersions along the Γ-K-X ([110]) line in (In,Fe)As:Be. The IB intensity obtained by rARPES is superimposed in the positive k_x region. The dispersions of the LH (circle), HH (square), and SO (rhombus) bands are also plotted. (Right) EDC at Γ (thin line) and Fe-3d PDOS (thick line). The colored areas denote the energy ranges of the Fe-3d IBs. (b) Band dispersion near E_F in InAs:Be, with the EDC at Γ on the right. (c) Band

dispersion in (In,Fe)As as well as (In,Fe)As:Be (Fig.(a)).

FIG.4. Band diagram of (In,Fe)As. (a),(b) Schematic DOS for ferromagnetic (In,Fe)As:Be and paramagnetic (In,Fe)As, respectively. DOS including the Fe 3d-derived IBs embedded in the VB and CB of the host InAs. The expected unoccupied Fe $3d_{\downarrow}$ states are also shown. (c),(d) Band diagrams for (In,Fe)As:Be and (In,Fe)As, respectively. Hybridization between Fe 3d $e_{\downarrow}$ and CB leads to the formation of α-IB and hybridization between Fe 3d $t_{2\downarrow}$ and VB to the formation of β-IB. Dash-dotted lines are the InAs-derived band dispersion without the hybridization. Electron occupation of CB pushes down the partially filled α-IB to be located below CBM, leading to the large spin-splitting Δ_{ex} of the CB.

FIG.5. APRES spectrum of (In,Fe)As obtained along the Γ-K-X line with *s* polarization. (a) APRES intensity along the Γ-K-X line obtained at $h\nu = 908$ eV. HH is the heavy-hole band of the host InAs. The incident photon energy for this measurement is of 908 eV as well as the ARPES spectrum taken with *p*-polarization shown in Fig. 2(c). (b) EDCs around the Γ point.

FIG.6. Fe L_3 resonant ARPES spectra taken with *s* polarization. The left and right panels are the off- and on-resonance spectra, respectively. IB is the Fe 3*d*-derived impurity band.

FIG.7. Spin-density-functional-theory calculation for an $In_{31}Fe_1As_{32}$ supercell. (a),(b) Spin-resolved band structure. The weight of Fe 3*d* is indicated by the size of red circles. The blue dash-dotted line is the energy position of E_F in the Be doped samples as observed experimentally. Note that as the E_F is shifted upwards, the Fe 3*d* $t_{2\downarrow}$ and $e_\downarrow$ bands are also shifted upwards and remain located above E_F due to Coulomb interaction as denoted by red arrows. The impurity band near E_F (α-IB) observed in the present work is considered to result from hybridization between the Fe $e_\downarrow$ bands and the CBM. (c) DOS for the up-spin (upper curve) and down-spin states (lower curve). (d) Partial density of states for Fe 3*d*.

FIG.8. Fermi surface mapping of an InAs:Be thin film. (a),(b) In-plane and out-of-plane FSM, respectively. The top right plots are momentum distribution curves (MDCs) along the k_x and k_y or k_z cuts across the Γ point (dashed lines), respectively.

FIG.9. Band dispersions of InAs:Be. (a) ARPES image plot along the Γ-K-X line obtained with *p* polarization. LH and SO denote the light-hole and split-off bands, respectively. (b) Energy distribution curves (EDCs) of the spectrum taken with *p* polarization. (c) ARPES image plot along the Γ-K-X line obtained with *s* polarization. HH denotes the heavy-hole band. (d) EDCs of the spectrum taken with *s* polarization. The ARPES images are 2nd derivatives of the ARPES intensities.

FIG.10. Band dispersions of paramagnetic (In,Fe)As. (a) ARPES image plot along the Γ-K-X line obtained with *p* polarization. (b) EDCs of the spectrum taken with *p* polarization. (c) ARPES image plot along the Γ-K-X line obtained with *s* polarization. HH denotes the heavy-hole band. (d) EDCs of the spectrum taken with *s* polarization. The ARPES images are 2nd derivatives of the ARPES intensities.

FIG.11. Fe L_3 resonant ARPES spectra of paramagnetic (In,Fe)As. (a),(b) rARPES spectra taken with *p* and *s* polarizations, respectively. The left and right panels are the off- and on-resonance spectra, respectively. IB denotes the impurity band.

Figure

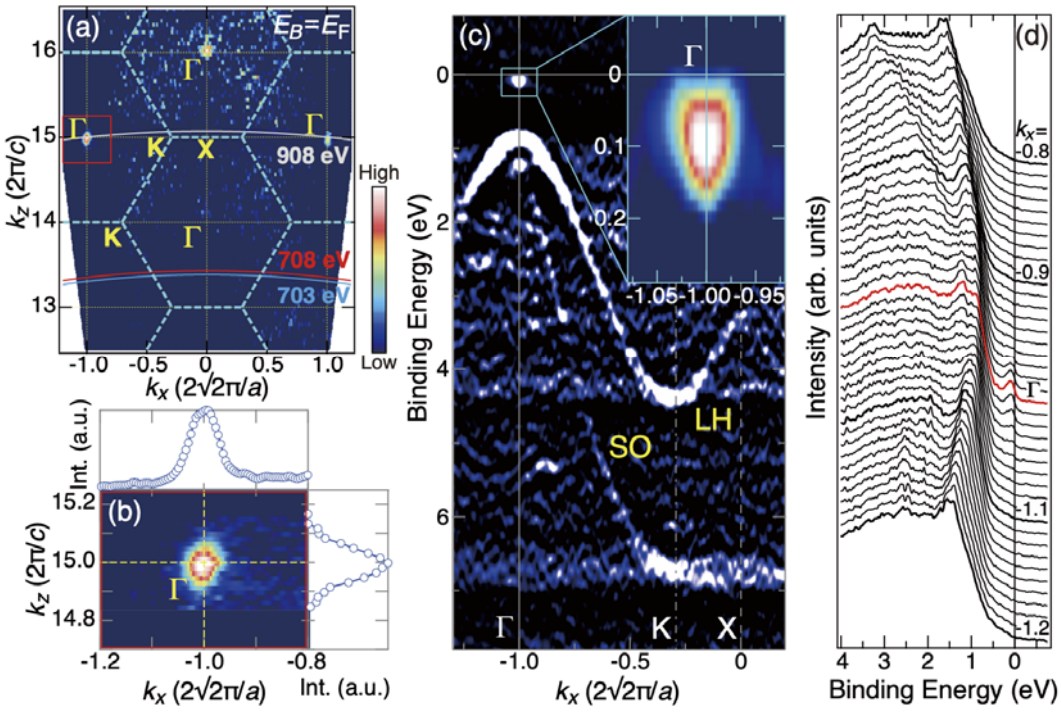
(a)
$E_B=E_F$
Γ
K
X
908 eV
708 eV
703 eV
High
Low
k_z (2π/c)
k_x (2√2π/a)
(b)
Int. (a.u.)
(c)
Binding Energy (eV)
LH
SO
(d)
Intensity (arb. units)
Binding Energy (eV)

Figure 1

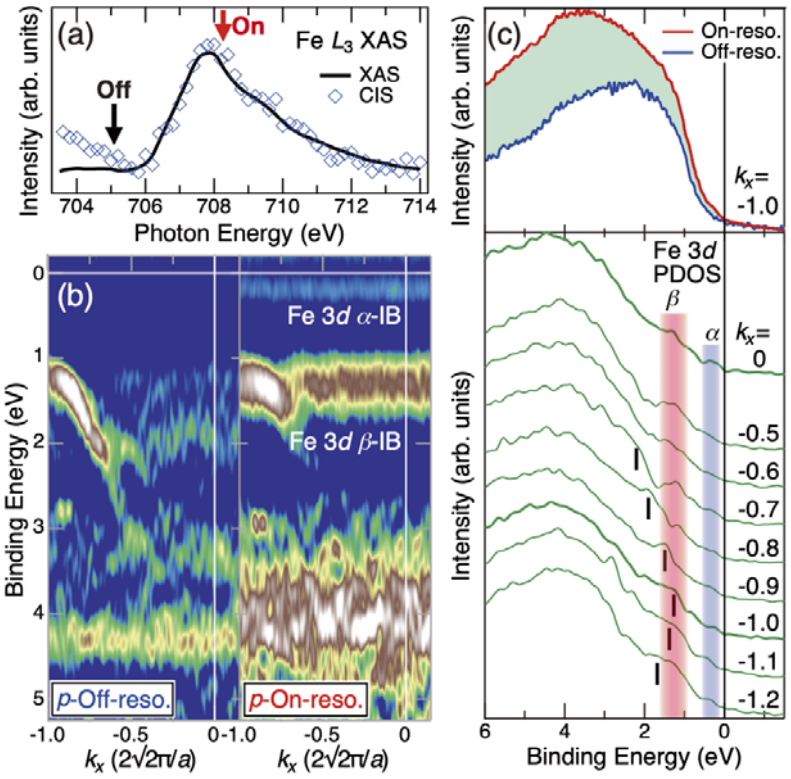

Figure 2

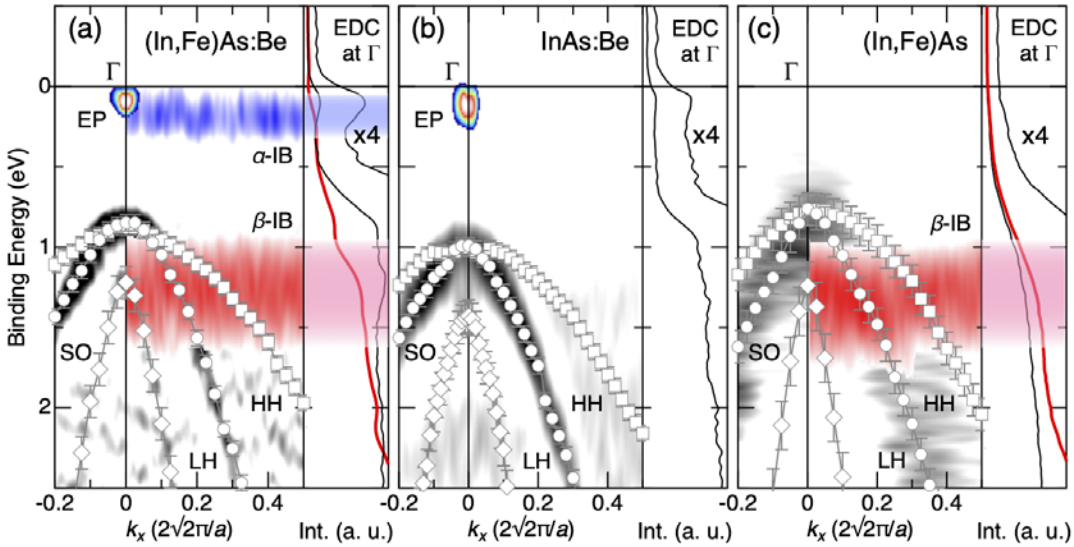

Figure 3

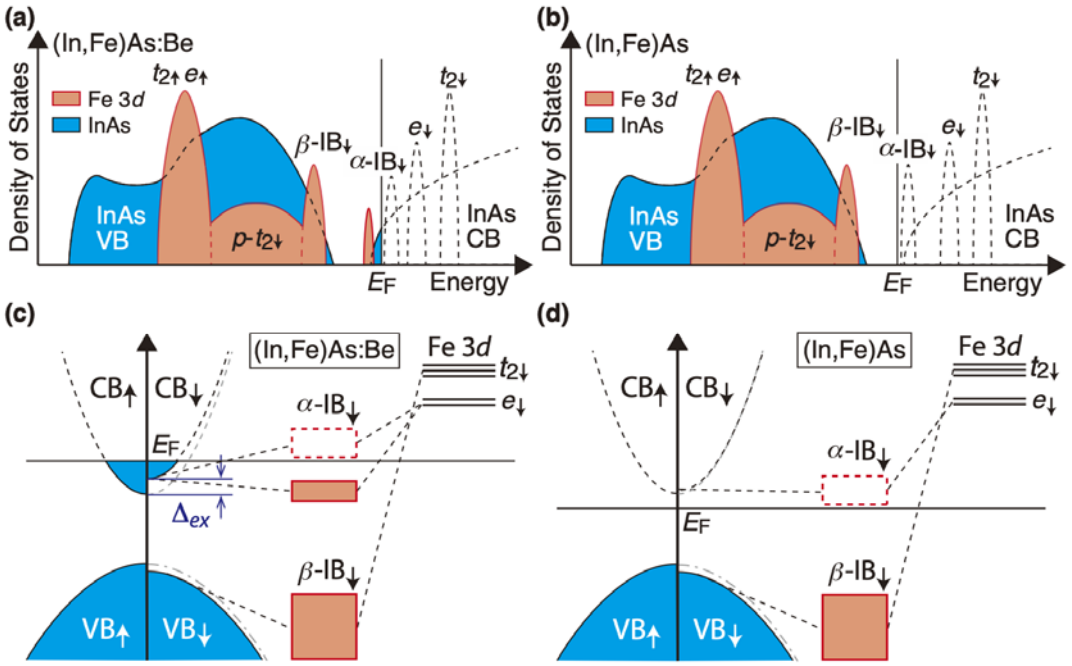

Figure 4

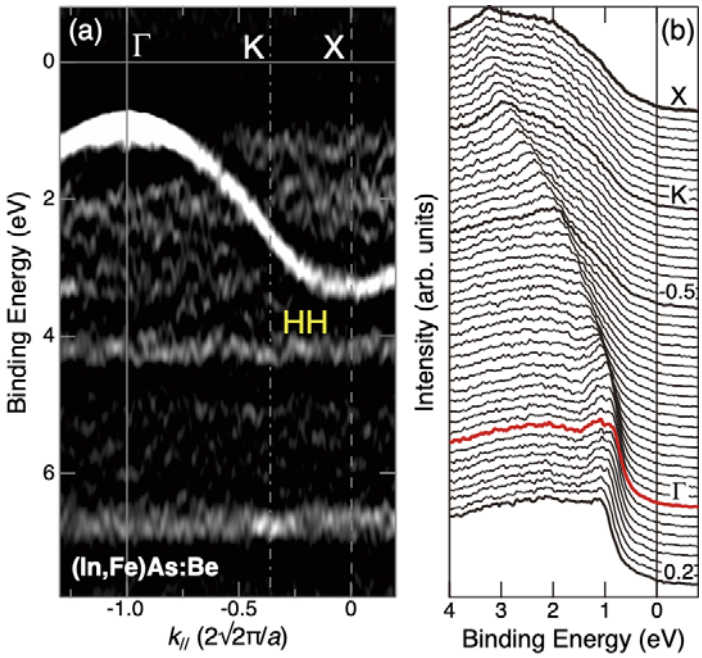

Figure 5

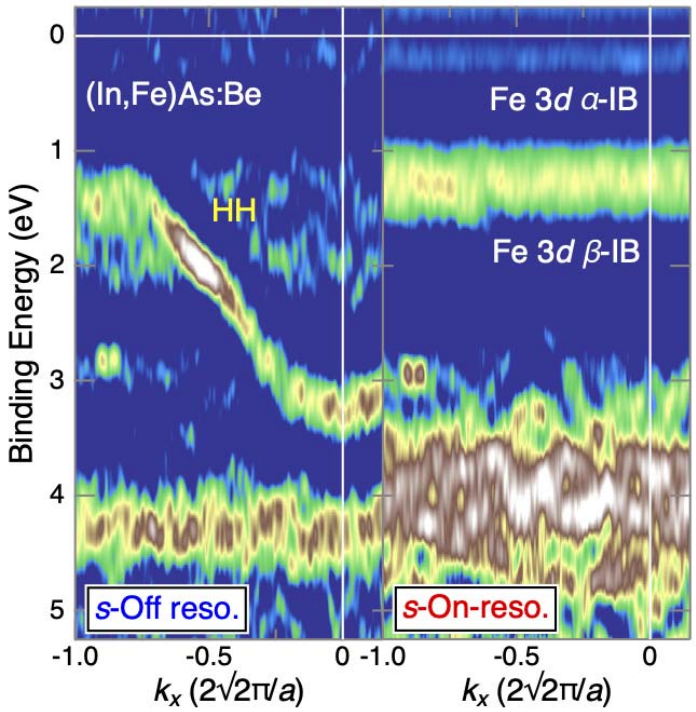

Figure 6

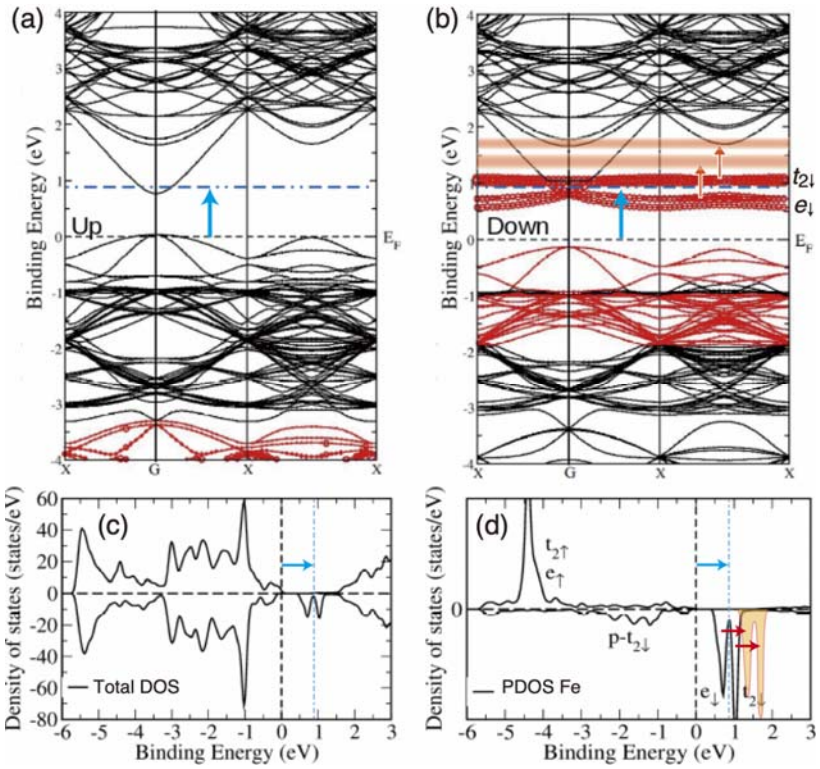

Figure 7

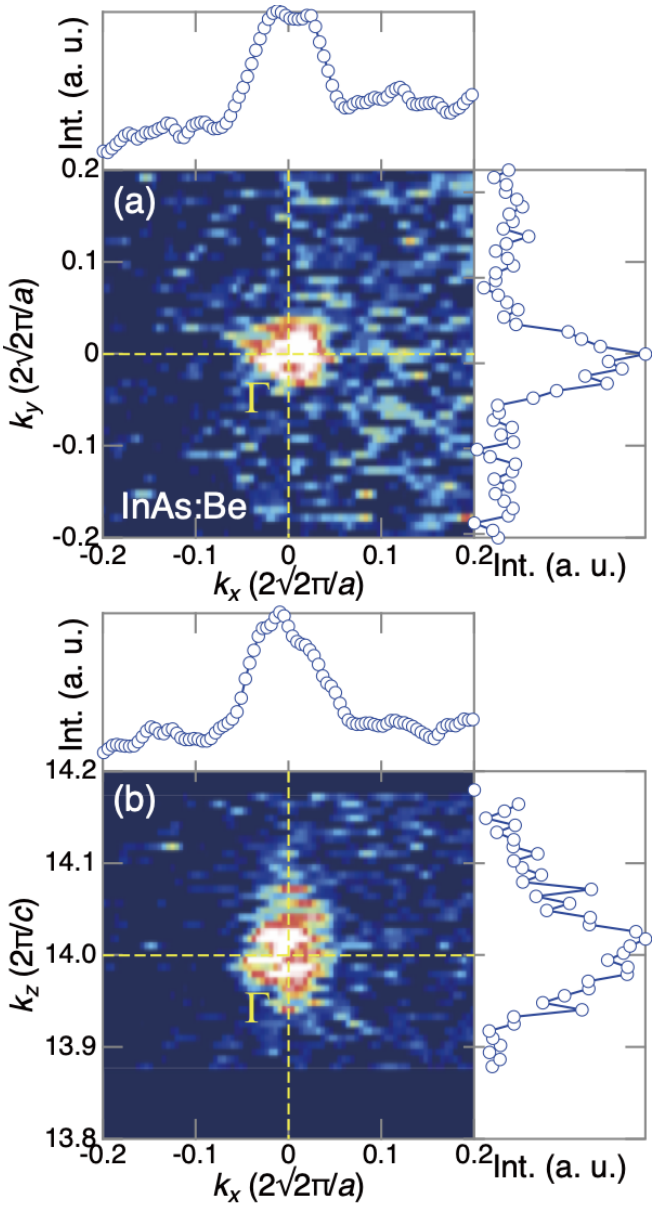
Int. (a. u.)
(a)
InAs:Be
Γ
k_y (2√2π/a)
k_x (2√2π/a)
Int. (a. u.)
0.2
0.1
0
-0.1
-0.2
Int. (a. u.)
(b)
Γ
k_z (2π/c)
k_x (2√2π/a)
Int. (a. u.)
14.2
14.1
14.0
13.9
13.8

Figure 8

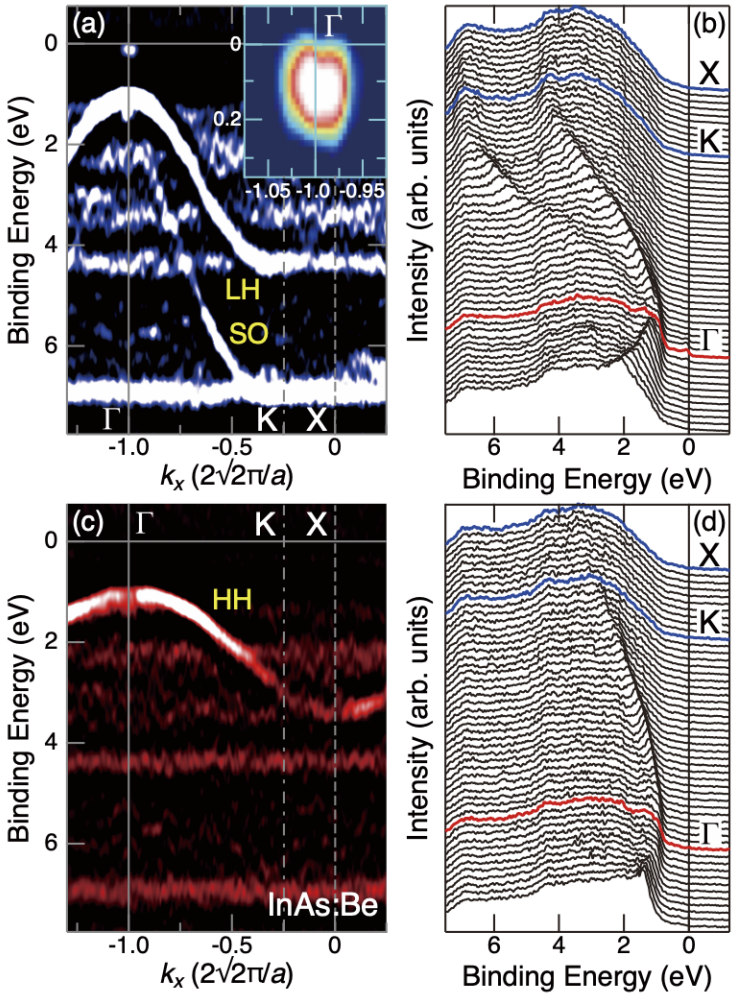
(a)
Γ
0
0.2
-1.05 -1.0 -0.95
LH
SO
Γ
K
X
Binding Energy (eV)
k_x (2√2π/a)
(b)
X
K
Γ
Intensity (arb. units)
Binding Energy (eV)
(c)
HH
InAs:Be
(d)

Figure 9

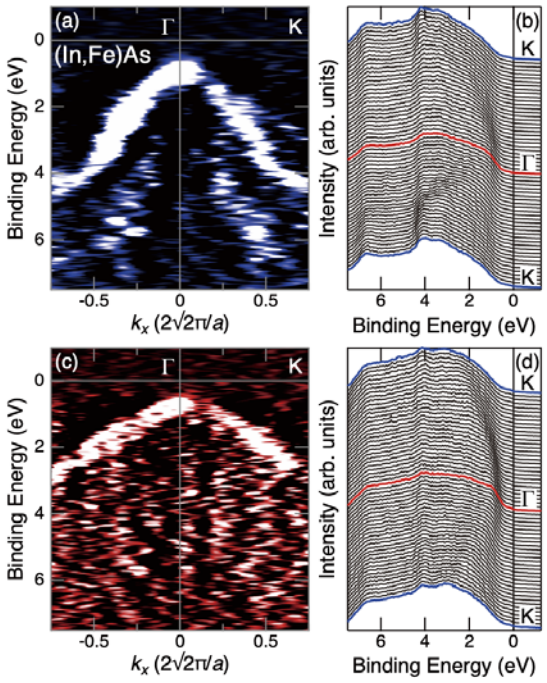
(a)
Γ
K
(In,Fe)As
Binding Energy (eV)
0
2
4
6
-0.5
0
0.5
k_x (2√2π/a)
(b)
K
Γ
K
Intensity (arb. units)
6
4
2
0
Binding Energy (eV)
(c)
Γ
K
Binding Energy (eV)
k_x (2√2π/a)
(d)
K
Γ
K
Intensity (arb. units)
Binding Energy (eV)

Figure 10

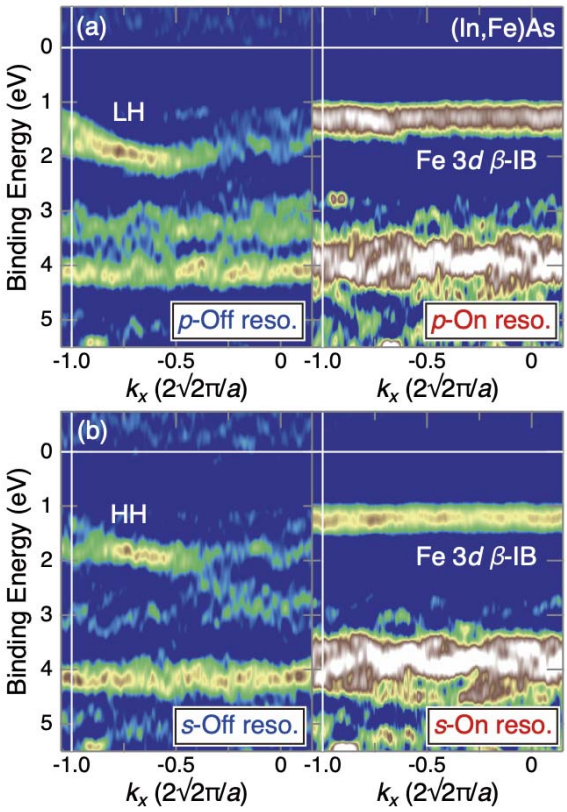
(a)
(In,Fe)As
LH
Fe 3d β-IB
p-Off reso.
p-On reso.
Binding Energy (eV)
0
1
2
3
4
5
-1.0
-0.5
0
k_x (2√2π/a)
(b)
HH
Fe 3d β-IB
s-Off reso.
s-On reso.

Figure 11